Energy 42 (2012) 81–93

Contents lists available at ScienceDirect

Energy

journal homepage: www.elsevier.com/locate/energy

Analysis of a new induction thermal converter for heating

Cezar Popa*, Radu Pentiuc

Stefan cel Mare University of Suceava, 13 Universitatii Street, RO 720229 Suceava, Romania

ARTICLE INFO

Article history:
Received 6 January 2011
Received in revised form
24 June 2011
Accepted 25 July 2011
Available online 1 September 2011

Keywords:
Electric-magnetic-thermal model
High efficiency
Induction converter
Massive winding
Residential building heating

ABSTRACT

The paper presents a new type of electro-thermal converter whose particular applications are used especially in heating materials or residential buildings. The converter is in fact a single-phase transformer with a massif secondary winding, calculated to work in short-circuit but in a stabilized thermal regime. The authors developed a coupled electric-magnetic-thermal numerical model that improved the calculation of power and temperature distribution in the secondary massive coil. Knowledge of local magnetic field intensity gives the possibility to evaluate local current density and volume distribution of electrical power in the material. The model can be used to predict evolution of coil temperature for different charges, secondary coil materials and for different geometrical designs. The equations used for the development of the numerical solutions are presented below, as well as some experimental results and practical applications.

© 2011 Elsevier Ltd. All rights reserved.

1. Introduction

Recent years have shown a continuous increase in number and power rating of induction equipment, accompanied by a demand for more accurate methods of predicting the electro-thermal performance of a system. Continued increase of industrial productivity and building management capabilities demand new heating equipments at low costs, highly efficient and reliable, ecological, with an efficient thermal control. Heat generation in static or rotating electric machines represents a direct consequence of the losses by Joule effect, magnetic hysteresis, eddy currents, friction between different structural elements. In order to ensure a normal temperature to operate the electrical machines, the thermal energy thus generated must be evacuated through the ventilation system into the environment and is considered as loss. Some possibilities to limit these losses are presented in [1]. For certain thermal applications one can design conversion devices that also perform conversion of thermal energy (corresponding to the losses) into useful energy used in thermal processes. This performance criterion is likely to offer a possible solution for a new class of induction heating equipment: transformer with secondary massive winding, Fig. 1a, asynchronous motors with secondary massive rotor, Fig. 1b, or combination of that two:

If an electrical transformer is considered, as in Fig. 1a (above), the absorbed electric energy W_{electric} is partly converted into useful electric energy transferred to a load $W_{\text{useful electrical}}$, and a part is lost in the magnetic core and the windings as thermal energy $\Delta W_{\text{thermal loss } c-w}$ that is transferred to the environment by natural or forced ventilation. Equally, if an asynchronous electric motor is considered, Fig. 1b (above), the electric energy given by the supply source W_{electric} is partly converted into useful mechanic energy $W_{\text{useful mechanical energy}}$, and a part is lost as thermal energy $\Delta W_{\text{thermal loss } r-s}$ in the rotor and stator circuit, respectively, in the moving mechanical subparts $\Delta W_{\text{mechanical loss}}$. The applications that need conversion of electric energy into thermal or even mechanical energy may use the converters whose operating principle is shown in Fig. 1a,b (below). The static converter transformer-type with massive secondary winding is designed to operate in short-circuit. It has been optimized so that the thermal energies generated in the secondary circuit $W_{\text{useful thermal sec}}$, in the magnetic core and in the primary winding $W_{\text{useful thermal } c-w}$ can be directed toward the thermal process. Similarly, through proper construction, the thermal energy $W_{\text{useful thermal } r-s}$ generated within the massive rotor of an asynchronous motor with exterior rotor can be used in the thermal process, thus achieving a dynamic converter of electric energy into useful mechanical $W_{\text{useful mechanical}}$ and thermal $W_{\text{useful thermal } r-s}$ energy. Another particularity of these electro-thermal converters is due to a special design of the massive secondary (heated load) which allows production of a magnetic field on the external surface.

There are many classic applications in textile and paper industry that use massive heating cylinders to diminish residual water percentage. This paper presents only the static converter with secondary massive winding, which can be used for residential

* Corresponding author. Tel.: +40 723 603108; fax: +40 230 524801.
E-mail addresses: cezarp@eed.usv.ro (C. Popa), radup@eed.usv.ro (R. Pentiuc).

0360-5442/$ – see front matter © 2011 Elsevier Ltd. All rights reserved.
doi:10.1016/j.energy.2011.07.046

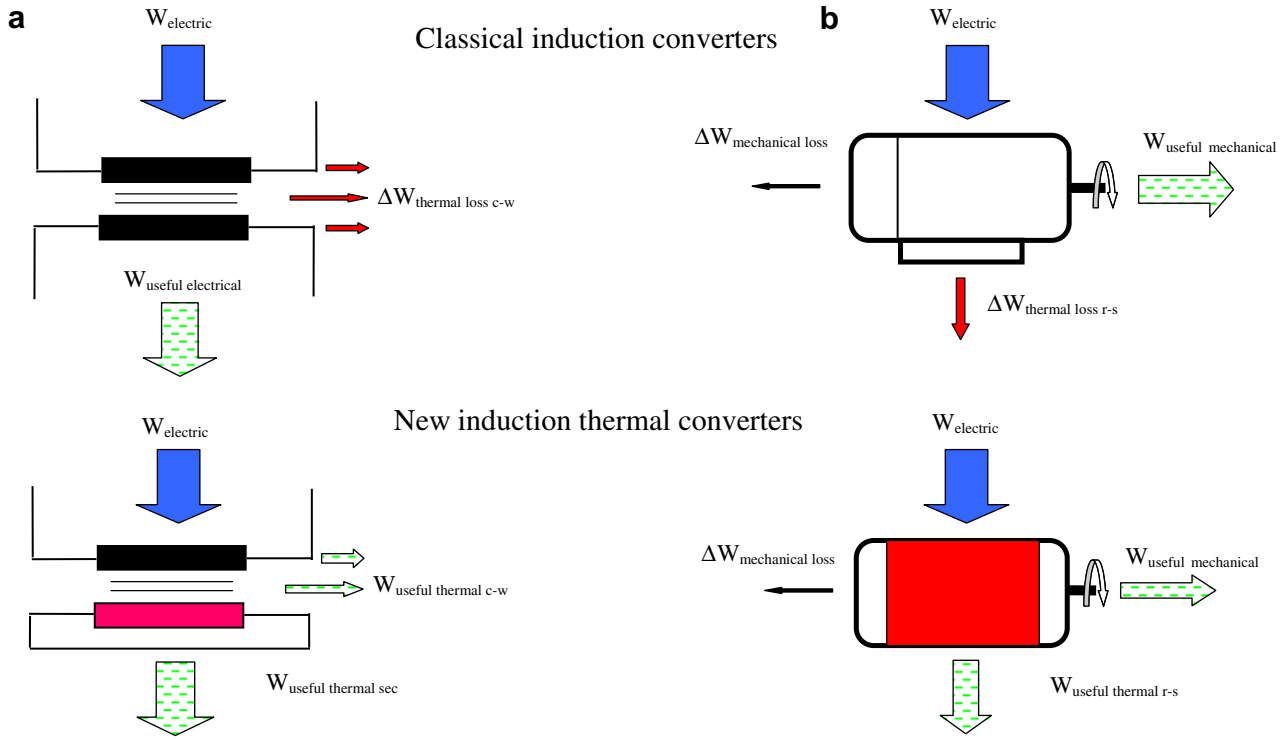


Fig. 1. Electric energy conversion systems type: a. static; b. dynamic.

heating applications or heating textures of materials to diminish residuals fluids [2], to improve speed of chemicals reactions [3–5] or to improve the products parameters in combined thermo-magnetic field (homogeneity, quality and stability of colors, fibers resistance) [6,7].

Design of that induction equipment with interior excitation demands an accurate method to determine the power generated in every element, especially in the heated load, and knowing that, one can evaluate the temperature distribution in the active zones. Correct induction process analysis can be done only if electro-magnetic and thermal phenomena are coupled in one unitary model [8]. Because, usually, the conditions for induction heating process are variable and some material properties are non-linear temperature-dependent, an analytical solution is in most cases impossible. Therefore, the numerical methods, as the finite-element method (FEM), was frequently used to solve 3-D models [9] and [10]. Recent studies [11] show that results difference between models using temperature-dependent and temperature independent parameters are 2…5% for working temperatures in the range of 60…160 °C. There are now on the market advanced finite-element software packages but numerous authors preferred to perform numerical calculations with computer programs they developed [12–15] in order to gain a better control on programs algorithms, physical parameters and for more flexibility in data transfer between different sub-models created for complex systems. We preferred the latter solution because our objective was to investigate the possibilities to achieve elevated converter efficiency for different possible geometries, materials and voltages. In this case we needed a simple and fast solution to change only the program variable input data. With FEM commercial software we must create new sub-models for each studied variant and sometimes the software has algorithm limitations. Simulation data for different static converter geometry and experimental results from tested prototypes were evaluated and discussed.

2. Numerical model of static converter

2.1. Electrical model

A numerical simulation method is proposed to accurately predict time variations for important electrical parameters in static converter assimilated to a single-phase transformer with closed massive secondary winding. Numerical simulation based on finite difference method uses classical electrical transformer equations and a proposed experimental function for magnetic core characteristic $\phi = f(i_m)$, including hysteresis loop and saturation:

$$\begin{aligned} u_1 &= N_1 \cdot \frac{d\phi}{dt} + R_1 \cdot i_1 + L_{1s} \cdot \frac{di_1}{dt}; \\ -u_2 &= N_2 \cdot \frac{d\phi}{dt} + R_2 \cdot i_2 + L_{2s} \cdot \frac{di_2}{dt}: \\ u_2 &= R \cdot i_2 + L \cdot \frac{di_2}{dt}; \\ N_1 \cdot i_1 + N_2 \cdot i_2 &= i_m \cdot N_1: \\ \phi &= f(i_m) \end{aligned} \tag{1}$$

where instantaneous primary exciting voltage is assumed to be $u_1 = \sqrt{2}U_1 \sin\omega t$, ω is the angular frequency of main source, N_1 and N_2 are primary and secondary windings turns, φ is the magnetic core flux, i_1 and i_2 are the windings currents, R_1 and R_2 are the windings electrical resistance, L_{1s} and L_{2s} are the leakage windings inductances, u_2 is the secondary voltage, R is the load resistance, L is the load inductance and i_m is the magnetization current.

For sampling k steep, in program simulation at an arbitrary moment $(t)_k$, instantaneous primary voltage is:

$$\begin{aligned} (t)_k &= k \cdot \Delta t \\ (u_1)_k &= \sqrt{2}U_1 \sin(\omega \cdot k \cdot \Delta t) \end{aligned} \tag{2}$$

For primary circuit and Δt sufficiently short (0.1 ms in our simulation program), the differential Eq. (1) can be expressed infinite difference form to get [16]:

$$N_1 \cdot \frac{(\Delta\phi)_k}{\Delta t} = (u_1)_k - R_1 \cdot (i_1)_k - L_{1s} \cdot \frac{(\Delta i_1)_k}{\Delta t}$$
$$(\Delta\phi)_k = (\phi)_k - (\phi)_{k-1}; (\Delta i_1)_k = (i_1)_k - (i_1)_{k-1} \quad (3)$$

For the secondary circuit in this particular case, closed massive secondary winding ($N_2 = 1$), we assume that impedance load is null ($R = 0$, $L = 0$) and transformer load is only secondary winding impedance, the differential Eq. (1) is rewritten as:

$$0 = \frac{(\Delta\phi)_k}{\Delta t} + R_2 \cdot (i_2)_k + L_{2s} \cdot \frac{(\Delta i_2)_k}{\Delta t} \quad (4)$$

where instantaneous secondary current is:

$$(i_2)_k = -\frac{N_2 \cdot \frac{(\Delta\phi)_k}{\Delta t} + L_{2s} \cdot \frac{(\Delta i_2)_k}{\Delta t}}{R_2} \quad (5)$$

respectively:

$$(\Delta i_2)_k = (i_2)_k - (i_2)_{k-1} \quad (6)$$

and finally, the form for secondary current:

$$(i_2)_k = -\frac{N_2 \cdot \frac{(\Delta\phi)_k}{\Delta t} - \frac{L_{2s}}{\Delta t} \cdot (i_2)_{k-1}}{R_2 + \frac{L_{2s}}{\Delta t}} \quad (7)$$

If magnetic flux value $(\phi)_k$ is known, we can evaluate the corresponding inrush current i_m from magnetic core characteristic $(i_m)_k = f((\phi)_k)$, and respectively the primary current $(i_1)_k$ of the converter:

$$(i_1)_k = (i_m)_k - (i_2)_k \cdot \frac{N_2}{N_1} \quad (8)$$

respectively:

$$(\Delta i_1)_k = (i_1)_k - (i_1)_{k-1} \quad (9)$$

Eq. (2)–(9) represent the base for the iterative process which allows evaluation of the most important electrical converter's parameters in time domain. To start the iteration process ($j = 1$) we must calculate $(\Delta\phi)_k$ and primary current variation $(\Delta i_1)_k$ in Eq. (3). To solve this problem, we define first initial conditions $(i_1)_0 = 0$, $(\phi)_0 = 0$, $(i_2)_0 = 0$ and for steep $k = 1$ at first iteration, R_1 and L_{1s} are neglected, to obtain an approximate value for magnetic flux:

$$(\phi)_k^{j=1} = -\frac{U_1}{\omega N_1} \cdot \cos(\omega k \Delta t)$$
$$(\Delta\phi)_k^j = (\phi)_k^j - (\phi)_{k-1}^j \quad (10)$$

Now, Eq. (7) can be solved, inrush current $(i_m)_k = f((\phi)_k)$ results from hysteresis characteristic and Eq. (8) can give the first value of the primary current. In respect to initialization, the iterative coupled electrical and magnetical subroutines can be started. On the second iteration, in Eq. (3) R_1, L_{1S} are not neglected, to obtain a more accurate value for $(\phi)_k^j$ and $(\Delta\phi)_k^j$. The iterative process is fast convergent, and it is stopped when the following condition is obtained:

$$\left|(i_1)_k^j - (i_1)_k^{j-1}\right| < \varepsilon_1 \quad (11)$$

where j is the number of necessary iterations to approximate $(i_1)_k$, into k steep, until specified error value ε_1 is achieved.

2.2. Magnetic field model

Because the electric and magnetic parameters are coupled we must solve both the mathematical models using numerical iterative techniques. Electrical parameters can be predicted with accuracy if first windings leakage inductance L_{1s}, L_{2s} used in Eq. (3) and (7) are known. In order to achieve that, some magnetic parameters like: windings leakage flux, differential permeability for different core zones, magnetic reluctances and magnetic field intensity in converter components must be derived from the equivalent magnetic circuit model. Equivalent magnetic circuits inside and outside window core are different. To determine the correct windings leakage inductances we must take into account the nature of the material it is made of (diamagnetic or ferromagnetic) and the distribution of the leakage magnetic flux according to the different reluctance ways of the equivalent magnetic circuit inside and, respectively, outside of the window magnetic core:

$$L_{1s} = \frac{N_1^2}{\Re_{1in}} + \frac{N_1^2}{\Re_{1out}}; \; L_{2s} = \frac{N_2^2}{\Re_{2in}} + \frac{N_2^2}{\Re_{2out}} \quad (12)$$

where $\Re_{1in}$ and $\Re_{2in}$ are magnetic reluctances that correspond to windings magnetic flux leakage inside window core, $\Re_{1out}$ and $\Re_{2out}$ are magnetic reluctances that correspond to windings magnetic flux leakage outside window core.

The share of the two areas depends on the thickness of the sheets package g_m and geometrical dimensions of the windings, as shown in Fig. 2.

According to Fig. 2, angles α_1, α_2 correspond to a half of the primary windings area, respectively secondary, found in the inner area of the window core and have the measurement given by the following:

$$\alpha_1 = 2 \cdot \arcsin \frac{g_m}{D_1 + g_1} \quad \alpha_2 = 2 \cdot \arcsin \frac{g_m}{D_1 + 2g_1 + 2g_a + g_2} \quad (13)$$

where D_1 is the primary winding inner diameter, g_1 is the primary winding thickness, g_a is the distance between exterior surface of primary winding (inductor) and interior surface of secondary and g_2 is the secondary winding thickness.

The share of windings in the inner window area in relation to their total surfaces is given by a form factor that corrects the leakage inductances corresponding to the windings L_{1s}, L_{2s}:

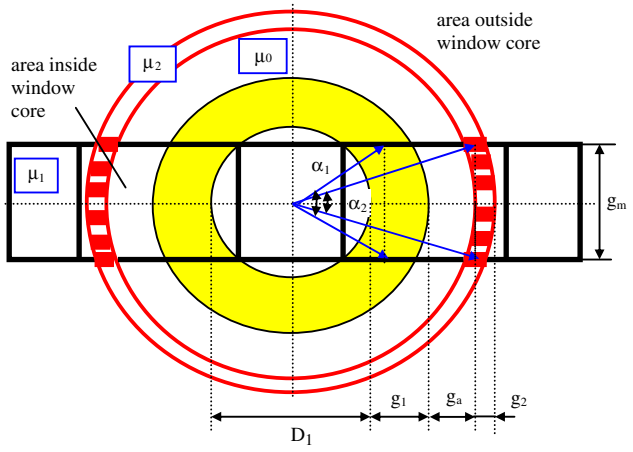


Fig. 2. System geometry to calculate share of windings inside and outside of window iron core.

$$k_{f1} = \frac{2\cdot\frac{\pi}{180}\cdot\alpha_1}{2\cdot\pi} = \frac{\arcsin\frac{g_m}{D_1+g_1}}{90} \quad k_{f2} = \frac{\arcsin\frac{g_m}{D_1+2\cdot g_1+2\cdot g_a+g_2}}{90} \tag{14}$$

For the magnetic equivalent circuit model the required input data are the geometric dimensions of the converter, magnetic core characteristic, magnetic flux ϕ (t_k), windings currents i_1 (t_k), i_2 (t_k) and the calculated output data are magnetic flux between principal convertor components and windings leakage inductances.

If material depth, when electromagnetic energy flows to a single part, is bigger than 3δ (depth of penetration of excitation wave), we can assume that it is equivalent to an infinite semi space with plane surface. To evaluate for the proposed static converter the components of a two-dimensional magnetic field, we can represent a winding section as a rectangular current distribution (curvature ignored) and use complex potential method in association with the method of images. In a two-dimensional magnetic field, the magnetic vector potential A has a single component about z co-ordinate [17]. The magnetic field intensity components H_y, H_z are real functions, in a field hypothetically without vertices and sources. Applying the images method for area outside window iron core (simplest study case), we obtain the geometric configuration presented in Fig. 3.

The significance of the presented elements: $\underline{r}$ is the distance between elementary element dz to point $P\,(Y, jZ)$ where magnetic field intensity is calculated, D_2 is the secondary winding inner diameter, g_{a1} is the distance between central column of magnetic core and interior surface of primary winding, h is the height of coil, $J = N\cdot i/h$ is the linear current density in windings or in windings images, N is number of windings turns, i_1 and i_2 are the currents in primary and secondary windings, $dI = J\ dz$ is the current into elementary element dz, μ_0 is the magnetic permeability of vacuum and μ_{r1} is the magnetic core relative permeability. Finite permeability of the core is corrected by adjusting the weight of linear current density for windings images, with a correction factor as indicated:

$$k_1 = \frac{\mu_{r1}-1}{\mu_{r1}+1} \tag{15}$$

To calculate magnetic field intensity in an aleatory point we must sum all components by y and z co-ordinate generated by windings and their images. The position vectors $\underline{r}$, in complex plane, which corresponds to windings, respectively to their images, are:

$$\begin{aligned}
\underline{r_1} &= (Y-g_{a1}-g_1)+j\cdot(Z-z) = \mathrm{Re}_1+j\cdot\mathrm{Im}_1\\
\underline{r_2} &= (Y-g_{a1}-g_1-g_a-g_2)+j\cdot(Z-z) = \mathrm{Re}_2+j\cdot\mathrm{Im}_1\\
\underline{r_1}' &= (Y+g_{a1}+g_1)+j\cdot(Z-z) = \mathrm{Re}_9+j\cdot\mathrm{Im}_1\\
\underline{r_2}' &= (Y+g_{a1}+g_1+g_a+g_2)+j\cdot(Z-z) = \mathrm{Re}_{10}+j\cdot\mathrm{Im}_1
\end{aligned} \tag{16}$$

Linear current densities taking into account the current sign and the correction factor k_1 given by Eq. (15) for every winding and their correspondent images are:

$$\begin{aligned}
J_1 &= \tfrac{N_1\cdot i_1}{h}\\
J_2 &= -\tfrac{N_2\cdot i_2}{h}\\
J_1' &= k_1\cdot\tfrac{N_1\cdot i_1}{h}\\
J_2' &= -k_1\cdot\tfrac{N_2\cdot i_2}{h}
\end{aligned} \tag{17}$$

In accord to Eq. (16) and (17) the components of magnetic field generated by every windings and images are:

$$\begin{cases}
H_y^{(1)} = -\dfrac{J_1}{4\cdot\pi}\ln\dfrac{\mathrm{Re}_1^2+A_1^2}{\mathrm{Re}_1^2+A_2^2}\\
H_z^{(1)} = \dfrac{J_1}{2\cdot\pi}\left[arctg\,\dfrac{A_1}{\mathrm{Re}_1}-arctg\,\dfrac{A_2}{\mathrm{Re}_1}\right]
\end{cases} \tag{18}$$

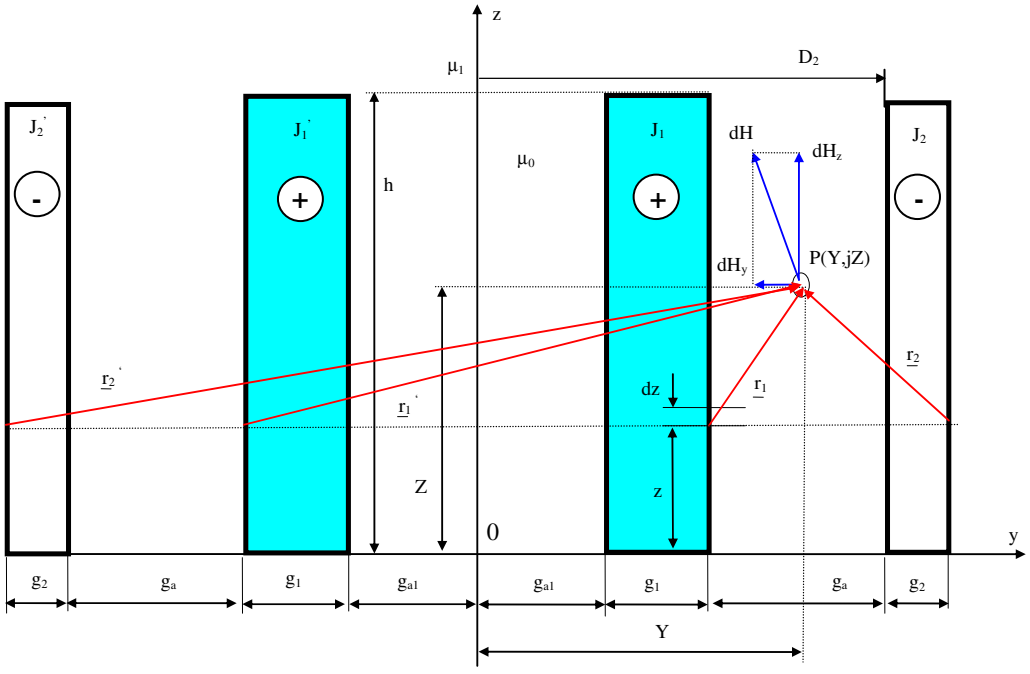


Fig. 3. Principle of calculating magnetic field for electro-thermal converter, for area outside window iron core.

$$\begin{cases} H_y^{(2)} = -\dfrac{J_2}{4\cdot\pi}\ln\dfrac{\mathrm{Re}_2^2+A_1^2}{\mathrm{Re}_2^2+A_2^2} \\ H_z^{(2)} = \frac{J_2}{2\cdot\pi}\left[arctg\dfrac{A_1}{\mathrm{Re}_2}-arctg\dfrac{A_2}{\mathrm{Re}_2}\right] \end{cases} \quad (19)$$

$$\begin{cases} H_y^{(1')} = -\dfrac{J_1'}{4\cdot\pi}\ln\dfrac{\mathrm{Re}_9^2+A_1^1}{\mathrm{Re}_9^2+A_2^2} \\ H_z^{(1')} = \frac{J_1'}{2\cdot\pi}\left[arctg\dfrac{A_1}{\mathrm{Re}_9}-arctg\dfrac{A_2}{\mathrm{Re}_9}\right] \end{cases} \quad (20)$$

$$\begin{cases} H_y^{(2')} = -\dfrac{J_2'}{4\cdot\pi}\ln\dfrac{\mathrm{Re}_{10}^2+A_1^2}{\mathrm{Re}_{10}^2+A_2^2} \\ H_z = \frac{J_2}{2\cdot\pi}\left[arctg\dfrac{A_1}{\mathrm{Re}_{10}}-arctg\dfrac{A_2}{\mathrm{Re}_{10}}\right] \end{cases} \quad (21)$$

with variables A_1 and A_2 defined by:

$$\begin{aligned} A_1 &= Z-h \\ A_2 &= Z \end{aligned} \quad (22)$$

The final components of magnetic field intensity in an aleatory point are:

$$\begin{cases} H_{y(Y,Z)} = H_y^{(1)}+H_y^{(2)}+H_y^{(1')}+H_y^{(2')} \\ H_{z(Y,Z)} = H_z^{(1)}+H_z^{(2)}+H_z^{(1')}+H_z^{(2')} \end{cases} \quad (23)$$

and magnetic field intensity modulus is:

$$|H| = \sqrt{H_y^2+H_z^2} \quad (24)$$

2.3. Thermal sources model

However, the magnetic flux intensity in a practical situation is not uniformly distributed, either across the air gap between windings, or along the length of the secondary massive winding. The approach used for low frequency magnetic field problem is to approximate uniform current distribution in primary winding. Non-sinusoidal driving currents and non-linear isotropic media are assumed. Fig. 4 presents magnetic field intensity excitation components and correspondent generated eddy currents in secondary massive winding.

To calculate power distribution in massive (non)ferromagnetic secondary winding, for non-sinusoidal currents excitation we must first calculate the currents harmonics level (for range 3 and 5 is generally sufficient, see Fig. 10). For each harmonics, the magnetic model gives local values for the components of magnetic field intensity at the interior surface of secondary winding. Now for the sinusoidal domain we may use Helmholtz equation to describe electromagnetic field in cylindrical massive wall:

$$\frac{\mathrm{d}^2\underline{H}}{\mathrm{d}r^2}+\frac{1}{r}\cdot\frac{\mathrm{d}\underline{H}}{\mathrm{d}r} = k^2\underline{H}; \quad k^2 = j\cdot\omega\cdot\mu_2\cdot\sigma \quad (25)$$

where H is the magnetic field intensity, r is the current radius for secondary winding, μ_2 is the secondary winding magnetic permeability and σ is the secondary electrical conductivity.

Finite-element analysis for magnetic field distribution demonstrates the possibility to consider cylindrical secondary winding in an axisymmetric field [9,11,14,18,19]. This approximation simplifies the spatial problem into a two-dimensional one in (r, z) coordinates with known magnetic field intensity components $\underline{H_{0z}}$, $\underline{H_{0y}}$ at secondary winding surface and along Oz axis. For Oz magnetic field component we have:

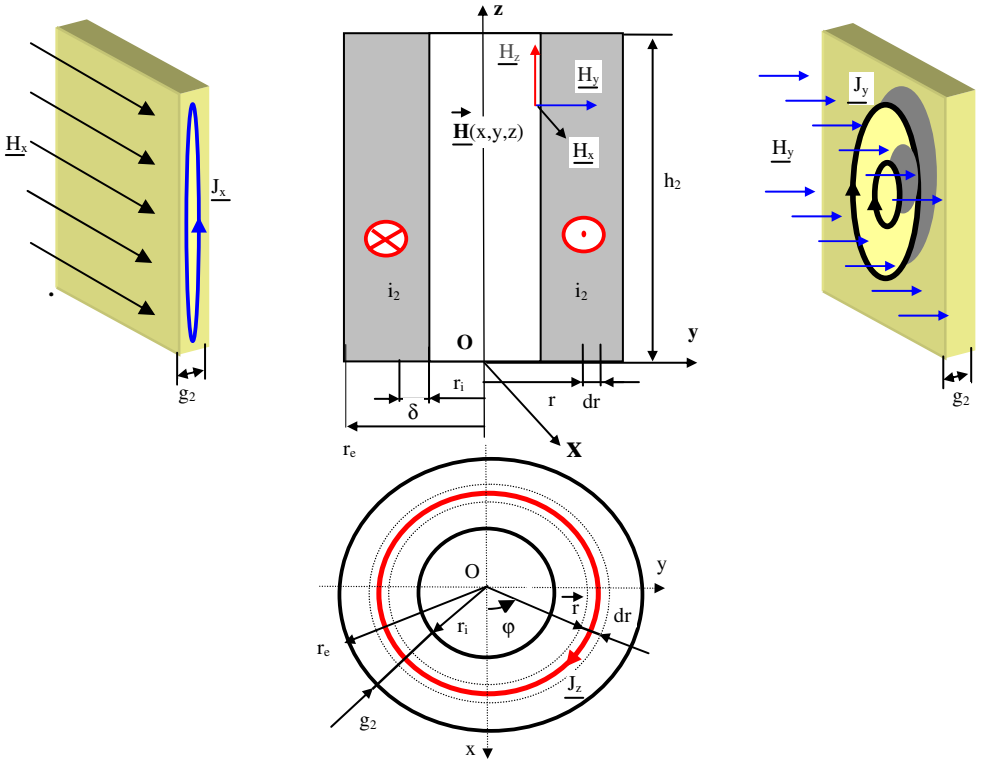


Fig. 4. Eddy currents components and their path in a massive winding.

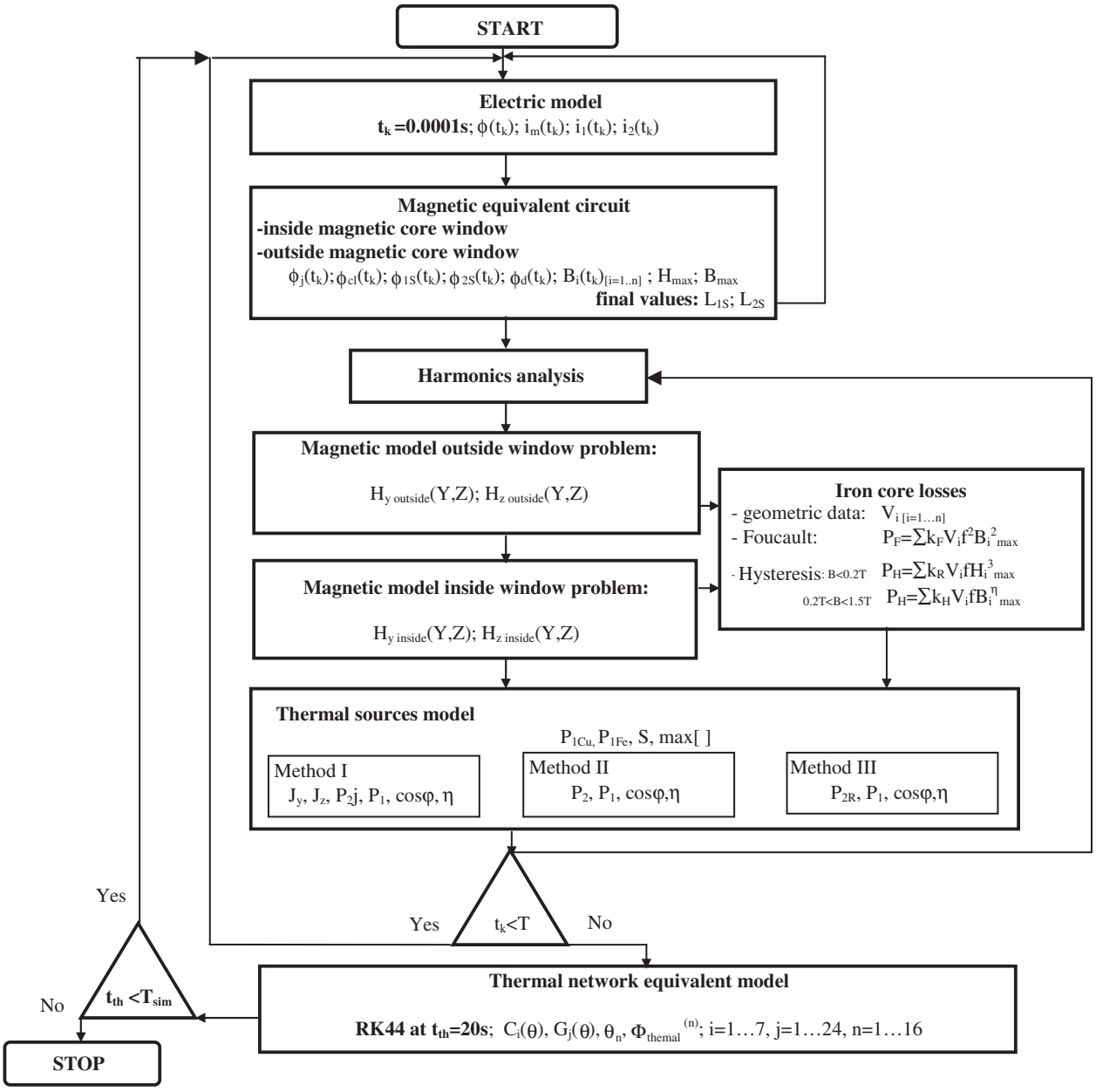


Fig. 5. Flowchart for integrated models, iterative algorithm.

$$\underline{H_z}(r) = \underline{H_{0z}}\frac{ber(mr)+j\cdot bei(mr)}{ber(mr_i)+j\cdot bei(mr_i)};\ m=\frac{\sqrt{2}}{\delta} \tag{26}$$

where r_i is the inner radius of secondary winding, r_e is the exterior radius, δ is the penetration depth and:

$$\begin{cases} k=\dfrac{1+j}{\delta};\ \delta=\sqrt{\dfrac{2}{\omega\cdot\mu_2\cdot\sigma}} \end{cases} \tag{27}$$

When: $r >> \delta$ (penetration depth), it is possible to use exponential development for Bessel functions with final solution:

$$\underline{H_z}(r) = \underline{H_{0z}}\frac{e^{-\frac{r}{\delta}}\cdot e^{-j\left(\frac{r}{\delta}-\frac{\pi}{8}\right)}}{2\cdot\sqrt{\pi\frac{r}{\delta}}}\cdot\frac{2\cdot\sqrt{\pi\frac{r_i}{\delta}}}{e^{-\frac{r_i}{\delta}}\cdot e^{-j\left(\frac{r_i}{\delta}-\frac{\pi}{8}\right)}} = \underline{H_{0z}}\cdot e^{-k(r-r_i)}\cdot\sqrt{\frac{r_i}{r}} \tag{28}$$

For a sufficiently small area we may consider local magnetic field intensity components constant, and current density $\underline{J_z}$ in a perpendicular plane to *Oz* axis, which can be expressed as:

$$\underline{J_z}(r) = rot_\phi \underline{H} = -\frac{\partial \underline{H_z}(r)}{\partial r} = \underline{H_{0z}}\cdot e^{-k(r-r_i)}\cdot\left(\sqrt{\frac{r_i}{r^3}}-k\cdot\sqrt{\frac{r_i}{r}}\right) \tag{29}$$

In addition, current density modulus is:

$$J_z(r) = \frac{H_{0z}}{\delta}\cdot e^{-\frac{r-r_i}{\delta}}\cdot\sqrt{\frac{r_i}{r}} \tag{30}$$

For $\underline{H_{0y}}$ component if secondary coil curvature is neglected ($r >> \delta$), the problem is reduced to a conductive plate in a perpendicular excitation field. For $\underline{J_y}$ component the current density modulus becomes:

$$J_y(r) = \frac{H_{0y}}{\delta}\cdot e^{-\frac{r-r_i}{\delta}}\cdot\sqrt{\frac{r_i}{r}} \tag{31}$$

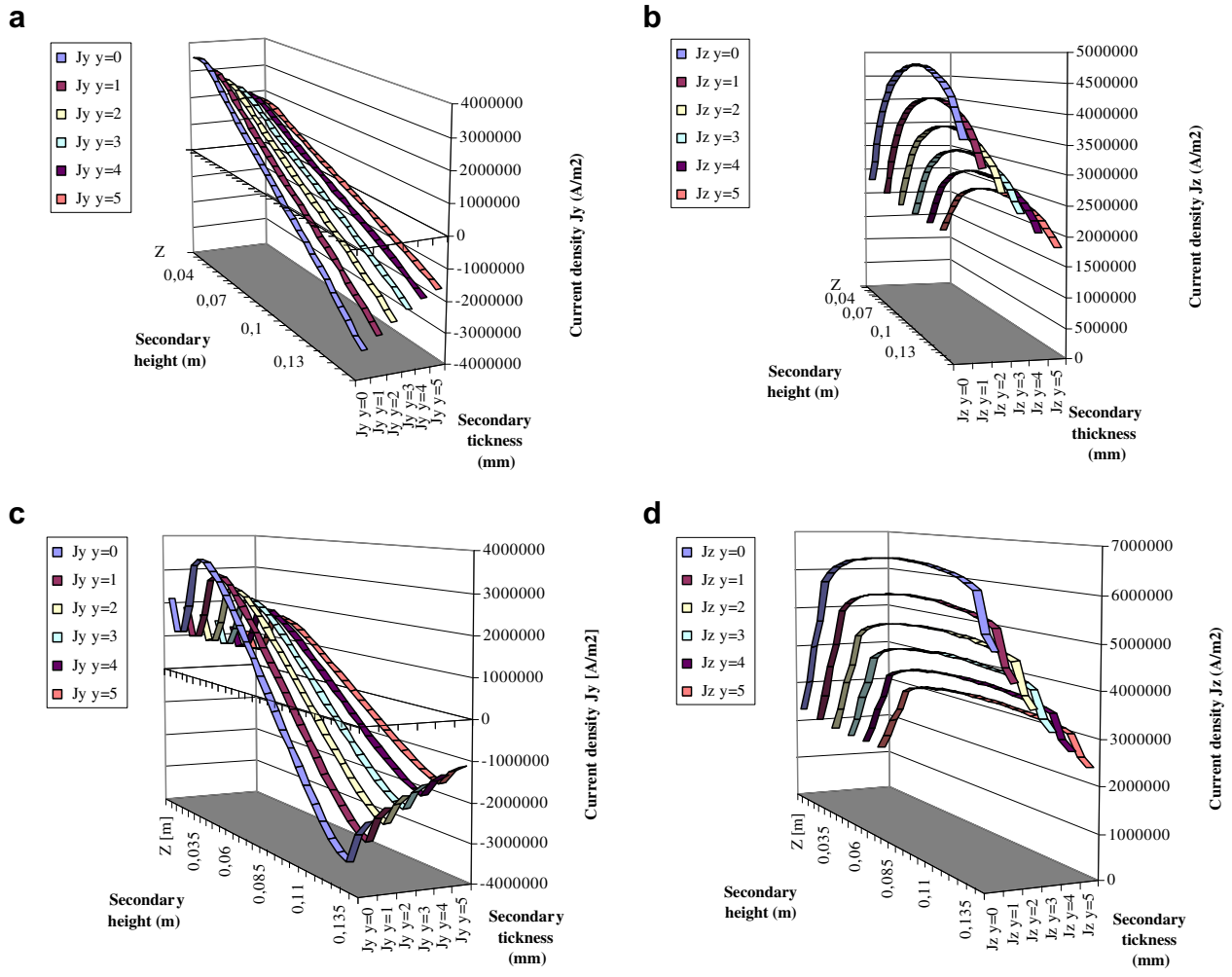


Fig. 6. Secondary current density distribution: a. J_y outside window; b. J_z outside window; c. J_y inside window; d. J_z inside window.

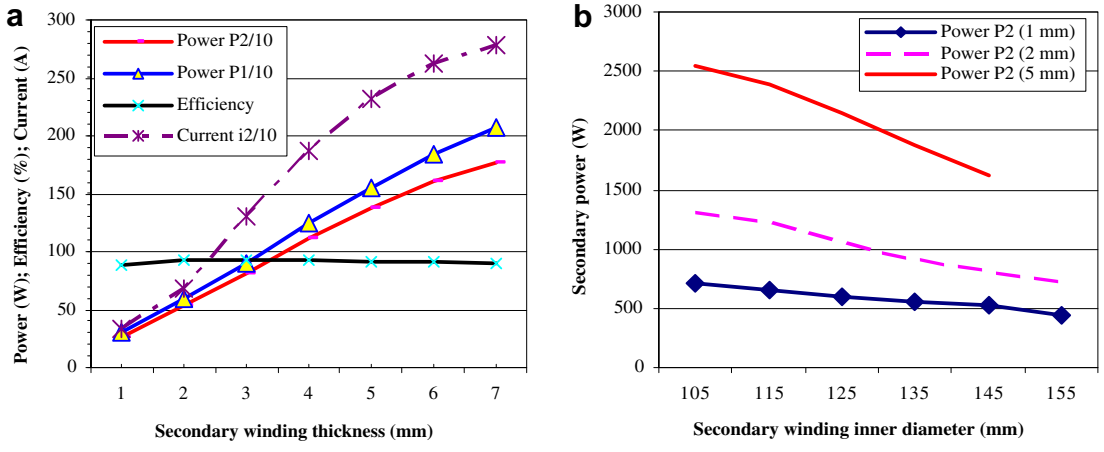


Fig. 7. The variation of the main electric parameters (simulation), massive iron secondary: a. modification of the secondary thickness; b. modification of the primary-secondary magnetic-clutch, $U_1 = 220$ V, $\theta_{secondary} = 25$ °C.

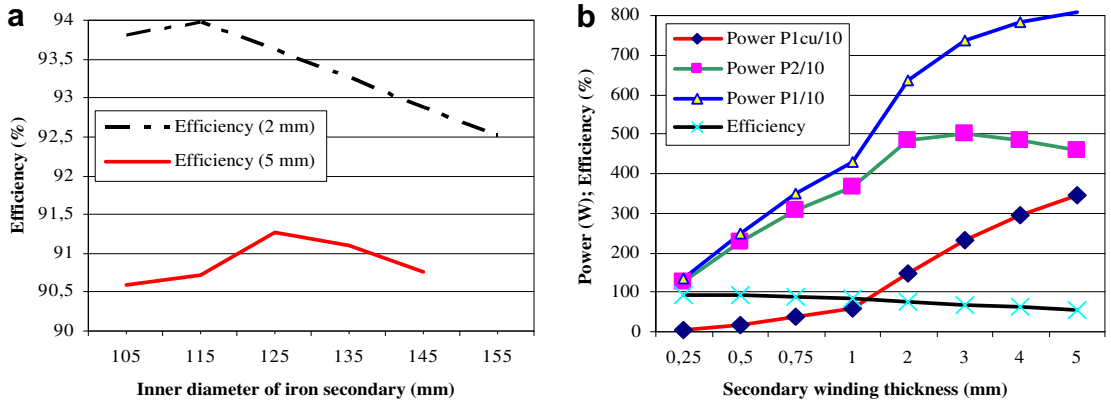


Fig. 8. Optimisation charts for converter efficiency function of system geometry, secondary winding material and electrical parameters: a. classically calculated electric efficiency, iron secondary; b. aluminum secondary.

For a cylindrical secondary region, with a height Δh sufficiently small to consider component of magnetic field intensity H_{0z} about constant, we can evaluate local active power, along Oy axis, with the equation:

$$P_{\text{axis}} = \int_V \rho \cdot J_{\text{axis}}(r) \cdot \mathrm{d}V = \int_{r_i}^{r_e} \rho \cdot J^2_{\text{axis}}(r) \cdot 2\pi r \cdot \mathrm{d}r \cdot \Delta h$$
$$= 2\pi \Delta h \rho_0 \cdot (1 + \alpha_R \cdot \theta_{\text{sec}}) \cdot \int_{r_i}^{r_e} r \cdot J^2_{\text{axis}}(r) \mathrm{d}r \qquad (32)$$

where ρ is the resistivity coefficient, α_R is the resistivity temperature coefficient, θ_{sec} is the secondary temperature at an arbitrary moment, $J_{\text{axis}}(r)$ is the current density in secondary winding, with variable values along Oy axis and V is the volume where local active power is calculated.

Eq. (32) can be solved numerically for a time interval Δt sufficiently short to consider secondary cylinder temperature θ_{sec} constant. For an infinitesimally length Δu situated at radius r_k in the secondary wall (along Oy axis), the local magnetic field intensity and current density can be assumed constant and Eq. (32) can be rewritten:

$$\Delta u = \frac{1}{n}(r_e - r_i)\ ;\ \Delta h = \frac{h}{n};\ n \geq 100 \text{ for } g_2 = 5 \ldots 10\,\text{mm} \qquad (33)$$

where n is the number of distinct calculus intervals on secondary winding and:

$$u_k = k \cdot \Delta u;\ r_k = r_i + u_k = r_i + g_2 \cdot \frac{k}{n};\ k = 0 \ldots n;\ n \in N \qquad (34)$$

$$P_{\text{axis}} = 2\pi \Delta h \rho_0 (1 + \alpha_R \cdot \theta_{\text{sec}}) \cdot \Delta u \left(J^2(u_0) \cdot r_0 + J^2(u_1) \cdot r_1 + \ldots \right.$$
$$\left. + J^2(u_k) \cdot r_k + \ldots + J^2(u_n) \cdot r_n \right) \qquad (35)$$

Because inside the magnetic core window the magnetic field intensity distribution is different from the magnetic field intensity outside of the window, we must solve the power distribution problem separately for each area (Fig. 2). To determine the total power induced in secondary winding we must sum the partial power along the considered axis Oz and Oy, using a numerical method. Another solution for assessment of thermal sources is to evaluate power developed in secondary winding by using a Poynting vector formula and to estimate power losses in different zones of iron core with data (magnetic flux density) resulted from magnetic equivalent circuit model, Fig. 5. To estimate thermal source for secondary winding we tested three subroutine program variants corresponding to the evaluation methods used:

I. Evaluation of local current density distribution with numerical integration of Eq. (35); II. Poynting vector method; III. Electric resistance approximation for secondary winding based on depth of

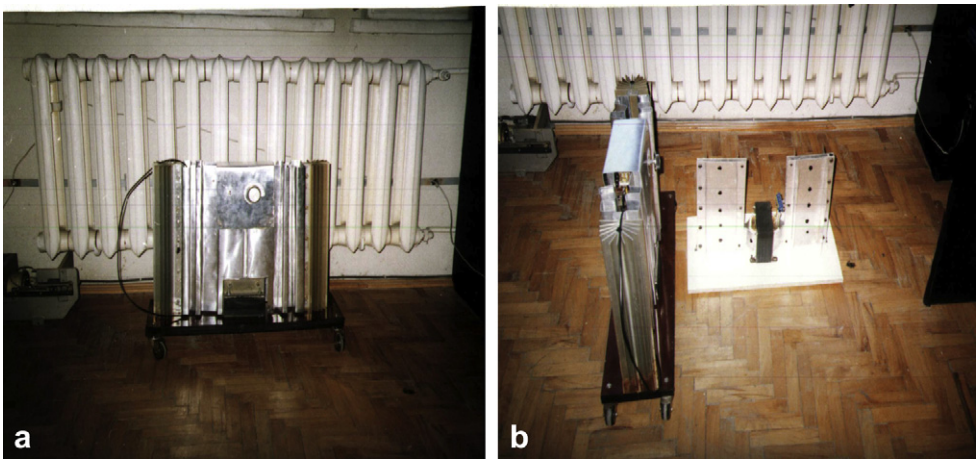


Fig. 9. Variants for electro – thermal converters: a. 1.600 W with temperature regulator; b. 1.600 W and 600 W.

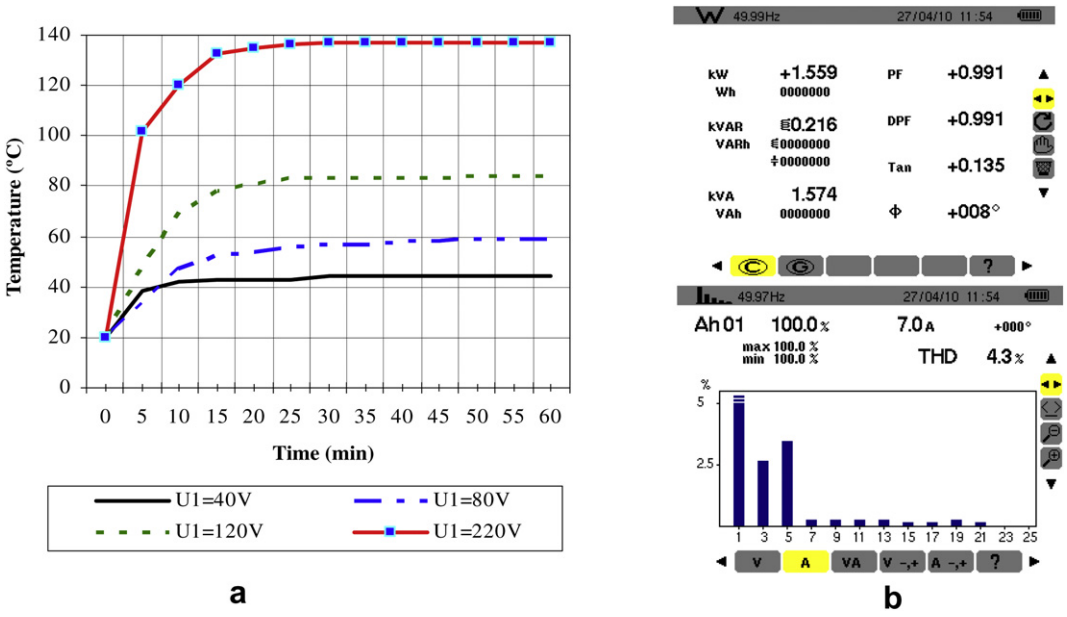


Fig. 10. Main parameters for induction electro-thermal converter with $P_{1max} = 1.600$ W: a. secondary temperature evolution for different voltages; b. power and harmonics analysis measurements for primary winding, $U_1 = 220$ V.

penetration. Simulation results for every method were compared with experimental data to validate the best solution.

2.4. Thermal model

The prediction of temperature rising in an electro-thermal converter presents many problems due to the fact that the heat transfer process is distributed over many surfaces. A thermal network model is proposed by dividing the converter into a number of finite subvolumes called nodes. Each node represents two thermal network elements, a temperature and a heat capacity. The temperature T, assigned to a node represents the average mass temperature of the subvolume and the heat capacity C is computed from the thermophysical properties of the subvolume material evaluated at the node temperature. Heat sources, windings and iron core losses, are functions of time and they are separately modeled, based on the results of electromagnetic simulations, Fig. 5. The boundary node (infinite heat capacity) is used to represent constant temperature sources within a thermal network (ambient temperature). Nodes are linked by thermal conductive conductances or by thermal radiative and convective conductances to the boundary node. All thermal conductances G are temperature-dependent [20] and [21]. The complete thermal network model is represented by sixteen nodes in total, seven of which represent the mean temperature of the elements (primary winding, secondary massive winding, thermal insulation between windings, field pole, core-central column, core-leg, core-yoke), while the remaining nine are secondary nodes [22]. The temperature rise for different parts of converter was calculated by a system of differential and algebraical equations, solved simultaneously in time domain using the Runge-Kutta 44 method to give the temperatures on all nodes. The simultaneous equations describing the steady state thermal network satisfy the conservation of heat flow balance:

$$\begin{cases} C_{11}\dfrac{d\Theta_1}{dt} + C_{12}\dfrac{d\Theta_2}{dt} + G_{11}\Theta_1 + G_{12}\Theta_2 = P \\ C_{21}\dfrac{d\Theta_1}{dt} + C_{22}\dfrac{d\Theta_2}{dt} + G_{21}\Theta_1 + G_{22}\Theta_2 = 0 \end{cases} \quad (36)$$

where Θ_1 is the vector of temperatures (main seven variables), Θ_2 is the vector of temperatures (secondary variables), C is the matrix of heat capacities resulted from thermal network model, G is the matrix of thermal conductances resulted from thermal network model and P is the vector of heat input from windings and iron core losses.

A C++ language computer program was written to solve the Eq. (36). Subsequently, by comparing the results given by the thermal model with the ones experimentally obtained, we can move on to the second stage, correction of thermal conductances values to minimize errors in the evaluation of temperatures. By coupling the electric, magnetic and thermal sources models with the thermal model, the reaction loop by temperature can be closed and thus analysis of the electro-thermal converter takes into account modification of material properties due to temperature and thermal transfer conditions to ambient. The integrated structure of the computer program that simulates function of the electro-thermal converter is presented in Fig. 5.

Validation of the converter model allows the study, in the time domain, of the temperatures evolution in the essential points and facilitates geometry optimization of constructive variants. The coupled subroutines were solved using an iterative procedure with two loops. On the first loop, the computer program calculates the electric, magnetic parameters and thermal sources for a period of main source equal to 20 ms, with 0.1 ms steep. On the second loop, the thermal model calculates the nodal temperature rises at every 20 s. In the thermal model, after each iteration the current temperatures were compared with the previous temperatures until the temperature difference between iterations was less than 0.1 °C for all the nodal temperatures rises. At each iteration loop the heat transfer coefficients were corrected for temperature. Current temperatures data are used in the first loop to correct temperature-dependent electric and magnetic parameters and heat sources.

3. Results and discussions

In order to validate the calculus model in the event of geometry variation, there have been carried out experimental determinations

with a special electro-thermal converter ($S = 2$ kVA, $U_1 = 110/220$ V, $N_1 = 115/310$ turns, $R_1 = 1.277\ \Omega$ at 20 °C, $L_{1s} = 2.777 \cdot 10^{-3}$ H) equipped with a secondary iron massive winding ($R_2 = 0.1981\ m\Omega$ at 20 °C, L_{2s} = variable, $g_2 = 5$ mm, $h = 0.135$ m) and respectively with an aluminum secondary winding ($R_2 = 0.05357\ m\Omega$ at 20 °C, $L_{2s} = 4.3 \cdot 10^{-8}$ H, $g_2 = 1$ mm, $h = 0.135$ m). Due to the iron core and ferromagnetic secondary winding nonlinearity, the simulation process in this case is more difficult and in order to validate the electromagnetic model we paid attention during the experimental phase to perform tests in different conditions and thus to improve the computer program models. The simulation results for magnetic field density were in good agreement with the experimental data obtained by using current probes (ten turns coils coupled to METRIX 3823 precision milivoltmeters) located in some relevant points along the iron core ($T1 \ldots T7$) and in secondary winding ($T2$m, $T2$up) in correspondence with similar points of equivalent magnetic circuit model; suplimentary, all results were confirmed by the FEM method (software package FLUX 2D). Table 1 presents, for different main sources, a comparison between the calculated and measured magnetic field density in test points. For iron core, and for main source values 50 V, 110 V and 220 V, the simulation errors are in range −7.63%…6.47% which represent a good result, taking into account that we considered in our model the magnetic core as a homogeneous structure and we neglected the air-gaps and interstitial air sheets. For the secondary winding, the magnetic field density calculated errors for the zone inside the window core are in the range of −4.08…3.31% and for the zone outside the window core they are a little bigger 4.69…7.59%, taking into account the inherent difficulties to appreciate the right magnetic flux ways for this zone in the equivalent magnetic circuit model.

These results validate the proposed magnetic equivalent model that can be used for analysis of static electro-thermal converter with ferromagnetic or diamagnetic secondary winding. Fig. 6 presents a simulation of current density distribution along the *Oz* and *Oy* axis, outside and inside core window, based on results obtained from the electromagnetic and thermal sources models. The difference between the current density distribution outside (Fig. 6a and b), inside window core (Fig. 6c and d) and the end effect on secondary winding are obvious.

The thermal sources model was validated by comparing experimental power P_{1exp} absorbed in primary circuit at different secondary winding temperatures θ_{sec} with simulations results P_{1sim} provided by each of the three calculus methods proposed. Power measurement was made with a power analyzer Chauvin Arnoux CA8334 with 1% precision. Partial results, for proposed secondary winding temperature range, are presented in Table 2.

The results in Table 2 show that the Poynting vector calculation method is the one that best modeled the real physical phenomena, being also the least influenced by the errors that affect the entry data given by the electric and magnetic models.

To provide a suitable comparison with the results of the thermal model, temperature measurements were made and considerable care was taken in the selection of the measurement points. We needed to embed the thermocouples at the points which coincide with the theoretical mean temperature points of each subvolume in the thermal network model. Choosing a location for the thermocouples was determined by the availability of positions. For data temperature acquisition from the experimental converter, we used a National Instruments NI USB-6008 acquisitions board, 6 thermocouples (two implanted in the primary winding, one in the iron core, two between thermal insulations and one on secondary winding) and 4 air temperature transducers to measure surface temperatures, coupled to Hanna thermometers (0.1 °C precision). Exchange thermal coefficients between different converter parts and ambient were adjusted in simulation program successively, to obtain the best fit between the measured and simulated temperatures, Table 3.

The good agreement between the simulated data and the measured temperatures demonstrates the validity of the proposed theoretical model which can be used to estimate the transient thermal behavior of the converter components and their final temperature for different geometry variants.

3.1. Converter analysis in case of system geometry variation

Geometry and position of the inductor in relation to the secondary winding have a significant influence on the transfer of the electromagnetic energy. As the electric efficiency η_e depends on a large number of interchangeable parameters and with various ratios, identifying the best geometry is significantly simplified in design stage if there are used proposed numerical models. In order to analyze the way in which power P_2, developed in the secondary winding may be increased, under the conditions of maintaining a satisfactory electric efficiency related to an acceptable thermal stress for the primary winding, the secondary thickness g_2 and the inner diameter D_2 has been modified.

The results of the simulations presented in Fig. 7a, show that for the established geometry of the converter with secondary made of iron, the best thickness for secondary winding is around the value of $g_2 = 4.5$ mm. After this value is surpassed, a drop can be noticed in the increase of the secondary power P_2, simultaneously with the increase of the losses inside the primary circuit P_{1Cu} and the drop of efficiency. The efficiency was calculated in the same way as for a classical transformer but in fact all losses transformed in warmth, in this converter, are useful components. The increase of the secondary power, for an optimal thickness of the secondary circuit, may be realized through the increase of the clutch factor between the primary circuit and the secondary one. When exploiting this possibility in practice, we have to take into consideration the fact that the diminution of the inner diameter D_2 of the secondary cannot be done without taking into account the thermal stress and necessary thickness of the thermal insulating layer, between primary and secondary circuits, depending on his characteristics. This restrictive condition imposes, according

Table 1
Experimentally and calculated magnetic flux density for thermal converter with iron secondary winding, 5 mm thickness.

	Zone	Iron core						Secondary winding (on iron)			
		Center	Yoke	Yoke	Yoke	Leg	Leg	Inside window		Ouside window	
U_1 (V)		B_c (T)	B_{Y1} (T)	B_{Y2} (T)	B_{Y3} (T)	B_{l1} (T)	B_{l2} (T)	$B_{seci\ middle}$ (T)	$B_{seci\ up}$ (T)	$B_{sece\ middle}$ (T)	$B_{sece\ up}$ (T)
	Test point	T1	T3	T4	T5	T6	T7	T2m	T2up	T2m	T2up
220	Simulation	1.030	0.653	0.593	0.591	0.557	0.530	0.757	0.352	0.539	0.202
	Experim	0.99	0.646	0.642	0.612	0.551	0.525	0.770	0.367	0.505	0.200
110	Simulation	0.515	0.326	0.296	0.295	0.268	0.242	0.334	–	0.223	–
	Experim.	0.488	0.312	0.310	0.293	0.264	0.237	0.315	0.152	0.213	0.085
50	Simulation	0.234	0.148	0.135	0.134	0.116	0.107	0.125	–	0.085	–
	Experim.	0.225	0.139	0.138	0.132	0.120	0.111	0.121	0.057	0.079	0.028

Table 2
Thermal sources model, experimental measurements and calculated powers P_{1sim}, for iron secondary winding, $g_2 = 5$ mm, $U_1 = 220$ V, $\theta_{ambient} = 20$ °C.

$\theta_{secondary}$ (°C)	20	30	40	50	60	70	80	90	100	120	140	160
i_{1exp}(A)	10.2	9.9	9.8	9.6	9.4	9.2	9.07	8.88	8.5	8.2	7.95	7.67
$P_{1exp.}$(W)	1840	1790	1760	1720	1700	1660	1630	1580	1540	1475	1400	1360
P_{1sim} Method I (W)	1870	1800	1755	1693	1665	1586	1540	1489	1448	1372	1301	1243
Errors (%)	1.63	0.55	−0.28	−1.56	−2.05	−4.45	−5.52	−5.75	−5.97	−6.98	−7.07	−8.60
P_{1sim} Method II (W)	1863	1802	1762	1709	1676	1612	1571	1528	1501	1418	1358	1333
Errors (%)	1.25	0.67	0.11	−0.64	−1.41	−2.89	−3.62	−3.29	−2.53	−3.86	−3.00	−1.98
P_{1sim} Method III (W)	1849	1727	1693	1644	1603	1564	1528	1493	1459	1397	1339	1286
Errors (%)	0.48	−3.51	−3.80	−4.41	−5.70	−5.78	−6.25	−5.50	−5.25	−5.28	−4.35	−5.44

to Fig. 7b, to choose the largest possible thickness for the secondary, in order to maximize secondary power. The simultaneous modification of the thickness g_2 and inner diameter of the secondary D_2, by using the numerical program, points out the possibility of improving the system geometry in order to maximize the value of the electric efficiency, Fig. 8a. Observing the same analysis criteria, Fig. 8b shows the influence of the geometrical dimensions in the case of a converter equipped with massive aluminum secondary. It has been pointed out the existence of the best value for the secondary thickness $g_2 = 0.3\ldots65$ mm for an imposed (by thermal stress) inner diameter $D_2 = 145$ mm and for secondary power in the range of interest $P_2 = 1500\ldots2500$ W. Surpassing this value determines the decrease in the converter efficiency and unjustified thermal stress of the primary circuit determined by an important increasing in primary winding power loss P_{1Cu}. As compared to the iron secondary, it has been established that for the same geometry, under the same conditions, the secondary power P_2 developed by the electro-thermal converter equipped with aluminum secondary is, on average, approximately 6…7 higher.

3.2. Experimental heating equipment

On the basis of the measurement made between November 2009 and March 2010 at a building situated in Suceava-Romania (with 25 apartments connected to a centralized heating network), equipped with a digital thermal energy metering system, type Schlumberger, we evaluated the necessary specific power to heat a square meter and, respectively a room, as shown in Table 4.

Three variants of induction heating equipment with maximum power 1.600 W, a normal heating radiator for an apartment room [23–27] have been made and tested. As compared to the electric heaters with resistance immersed in oil, or those with open flame (gas), the induction heating equipment has a few advantages that may impose it in making the heating installations:

- it is not dangerous when overheated, because of: the limitation of the control angle of the variable voltage regulator and the sizing of the radiating surface so that the maximum working temperature does not exceed 85–90 °C, at a surrounding temperature of 20 °C;
- it does not present any explosion and fire hazard if the variable voltage regulator breaks (heater with electric resistance immersed in oil) or any gas leak hazard (heater with open flame);
- it does not modify the oxygen content in the room where it is mounted (the heater with open flame);
- the developed power/size-weight ratio is very good (see Fig. 9);
- the total exploitation duration is compared to that of the steel heating equipment used in the district heating networks (risk of water leak in apartment), but at a reduced price for the same radiated power;
- it does not present any electric shock danger through direct touch of the secondary radiant surface;
- the maintenance costs are insignificant, as only periodic general overhauls are necessary.

Fig. 9 presents the option of heating equipment with maximum power of 1.600 W, devised for heating dwelling spaces, equipped with electronic power control which offers the possibility to integrate this converter in an automatic thermal system.

The experimental determinations were carried out for three types of induction heating equipment:

- with electrical power $P_1 = 600$ W, $U_{1max} = 110$ V, radiant surface $S_r = 0.2$ m^2, $\theta_{max} = 200$ °C, without temperature regulator;
- with electrical power $P_1 = 1.600$ W, $U_{1max} = 220$ V, radiant surface $S_r = 1.2$ m^2, $\theta_{max} = 140$ °C, with temperature regulator and control of top primary winding temperature, for room area around 30…35 m^2;
- with maximum electrical power limited in automatic mode at 460 W, and in manual mode at 600 W: $U_{1max/automat} = 120$ V,

Table 3
Thermal model, measured secondary temperature $\theta_{secondary\ exp}$ and calculated $\theta_{secondary\ sim}$, for iron secondary, $g_2 = 5$ mm, $U_1 = 220$ V, $\theta_{ambient} = 24$ °C.

t (s)	0	20	40	60	80	100	120	140	160	180	200	220
$P_{1exp.}$(W)	1820	1780	1700	1620	1492	1460	1402	1368	1336	1304	1268	1240
P_{1sim} Method II (W)	1840	1764.6	1595.5	1533	1476.6	1425.8	1380.1	1339	1302	1268.7	1238.6	1211.3
$\theta_{secondary\ exp}$ (°C)	24	41.2	66.1	90	111.5	131.8	150	167.3	184	198.9	214.6	228.7
$\theta_{secondary\ sim}$ (°C)	24	42.36	65.64	87.90	109.12	129.28	148.39	166.49	183.60	199.76	215.03	229.44
Temp. errors (%)	0	2.81	−0.69	−2.33	−2.13	−1.91	−1.07	−0.48	−0.22	0.43	0.20	0.32

Table 4
Necessary heating power for a building (non-isolated walls) with 8 floor, heating surface, $S = 1340$ m^2, winter average ambient temperature for Suceava $\theta_w = -4$ °C.

Months	11.2009	12.2009	01.2010	02.2010	03.2010
$P_{average}$ (kW)	68.38	76.95	82.44	80.93	61.42
P_{max} (kW)	82	94	108	103	86
$P_{specific}$ (W/m^2)	51.02	57.42	61.52	60.39	45.84
P_{room} (W) $S_{room} = 14/25$ m^2	714/1275	803/1435	861/1538	845/1510	641/1146

$\theta_{max/automat} = 84\ ^{\circ}C$, $U_{1max/manual} = 150$ V, $\theta_{max/manual} = 92\ ^{\circ}C$, radiant surface $S_r = 1.2\ m^2$, with temperature regulator designed to work in automatic systems for apartment temperature control.

For the last case, the maximum power of the 1.600 W heating equipment was electronically limited to approximately 600 W, so that the temperature of the radiating surface does not surpass the safety temperature of 92 °C, when there is the danger of causing fires in the event of direct contact with other objects. Temperature evolution of secondary winding, for different voltages of main source, based only on self-regulating natural process of convection and radiation to ambient is presented in Fig. 10a and demonstrates another possibility to limit the secondary temperature by an adequate design of winding surface. Thus the power of the heating equipment may be increased to the maximum value of 1600 W, and keeping the temperature of the radiating surface at the safety level (92 °C) by adequately increasing the secondary's radiant surface.

The analysis of power absorbed in primary winding made with a power analyzer CA8334, and presented in Fig. 10b, confirms, for this type of converter too, that current excitations are non-sinusoidal (THD = 4.3%) and harmonics for range 5 and 3 are the most important, with a relative level of 3.5% respectively 2.55% and it is compulsory to take into consideration their contribution in the simulation program in order to correctly assess the power of the thermal sources.

As it can be made of iron or aluminum, the converter's secondary can be designed to be an integrant part of the building's wall structure, as ornamentation of the heated areas, thus gaining more space and extra environmental aesthetics. Due to the constructive limits, this solution could not yet be put into practice in laboratory.

4. Conclusions

The variants of electro-thermal converters have allowed a successive improvement in the construction and thermal efficiency so that the final solutions presented represent competitive alternatives in relation to the classical heating solutions used at present. The adopted solutions made possible the creation of a simple, controllable and reliable thermal converter, whose inherent losses caused by operation are used in heating processes to obtain elevated efficient use of energy.

References

[1] Saidur R. A review on electrical motor energy use and energy savings. Renewable and Sustainable Energy Reviews 2010;14(3):877–98. Article | PDF (1132 K) | Wiew Record in Scopus | Cited By in Scopus (5).

[2] El-Amin MF. Combined effect of internal heat generation and magnetic field on free convection and mass transfer flow in a micropolar fluid with constant suction. Journal of Magnetism and Magnetic Materials 2004;270(1–2):130–5. Article | PDF (211 K) | Wiew Record in Scopus | Cited By in Scopus (8).

[3] Henninger F, Friedrich K. Production of textile reinforced thermoplastic profiles by roll forming. Composite Part A: Applied Science and Manufacturing 2004;35(5):573–83. Article | PDF (994 K) | Wiew Record in Scopus | Cited By in Scopus (6).

[4] Liu Q, Schlangen E, Garcia A, van de Ven M. Induction heating of electrically conductive porous asphalt. Construction and Building Materials 2010;24(7): 1207–13. Article | PDF (514 K) | Wiew Record in Scopus | Cited By in Scopus (1).

[5] Barthélémy B, Devillers S, Minet I, Delhalle J, Mekhalif Z. Induction heating for surface triggering styrene polymerization on titanium modified with ATRP initiator. Journal of Colloid and Interface Science 2011;354(2):873–9. Article | PDF (693 K).

[6] Valente Nabais JM, Carrott PJM, Ribeiro Carrott MML. From commercial textile fibres to activated carbon fibres: chemical transformations. Materials Chemistry and Physics 2005;93(1):100–8. Article | PDF (582 K) | Wiew Record in Scopus | Cited By in Scopus (5).

[7] Li SY, Wang BW, Weng L, Zhou Y, Sun Y, Huang WM. The effect of magnetic field heat treatment on magnetostriction of Terfenol-D 2-2 composites. Journal of Magnetism and Magnetic Materials 2008;320(6):806–9. Article | PDF (163 K) | Wiew Record in Scopus | Cited By in Scopus (2).

[8] Bay F, Labbé V, Favennec Y, Chenot JL. A numerical model for induction heating processes coupling electromagnetism and thermomechanics. International Journal for Numerical Methods in Engineering 2003;58(6):839–67. Full Text via CrossRef | Wiew Record in Scopus | Cited By in Scopus (29).

[9] Drobenko B, Hachkevych O, Kournyts'kyi T. A mathematical simulation of high temperature induction heating of electroconductive solids. International Journal of Heat and Mass Transfer 2007;50(3–4):616–24. Article | PDF (367 K) | Wiew Record in Scopus | Cited By in Scopus (6).

[10] Kurose H, Miyagi D, Takahashi N, Uchida N, Kawanaka K. 3-D eddy current analysis of induction heating Apparatus considering heat Emission, heat Conduction and temperature Dependence of magnetic Characteristics. IEEE Transaction on Magnetics 2009;45(3):1847–50. Full Text via CrossRef | Wiew Record in Scopus | Cited By in Scopus (7).

[11] Kranjc M, Zupanic A, Miklavcic D, Jarm T. Numerical analysis and thermographic investigation of induction heating. International Journal of Heat and Mass Transfer 2010;53(4):3585–91. Article | PDF (367 K).

[12] Sadeghipour K, Dopkin JA, Li K. A computer aided finite element/experimental analysis of induction heating process of steel. Computers in Industry 1996; 28(3):195–205. Abstract | Wiew Record in Scopus | Cited By in Scopus (23).

[13] Favennec Y, Labbé V, Bay F. Induction heating processes optimization a general optimal control approach. Journal of Computational Physics 2003; 187(1):68–94. Abstract | Wiew Record in Scopus | Cited By in Scopus (24).

[14] Kawaguchi H, Enokizono M, Todaka T. Thermal and magnetic field analysis of induction heating problems. Journal of Materials Processing Technology 2005; 161(1–2):193–8. Article | PDF (505 K) | Wiew Record in Scopus | Cited By in Scopus (15).

[15] Hansson S, Fisk M. Simulation and measurements of combined induction heating and extrusion processes. Finite Elements in Analysis and Design 2010; 46(10):905–15. Article | PDF (1081 K).

[16] Lin CE, Cheng CL, Huang CL, Yeh JC. Investigation of Magnetising inrush current in transformers. I. Numerical simulation. IEEE Transactions on Power Delivery 1993;8(1):246–54 [Full Text via CrossRef].

[17] Hortopan G. Ecranarea electromagnetica in tehnica curentilor intensi. Bucuresti: Ed. Tehnica; 1990 [Romanian].

[18] Chaboudez C, Clain S, Glardon R, Mari D, Rappaz J, Swierkosz M. Numerical modeling in induction heating for axisymmetric geometries. IEEE Transaction on Magnetics 1997;33:739–45 [Full Text via CrossRef].

[19] Bermüdez A, Rodriguez R, Salgado P. Numerical solution of eddy currents problems in bounded domains using realistic boundary conditions. Computer Methods in Applied Mechanics and Engineering 2005;194(2–5):411–26. Article | PDF (473 K) | Wiew Record in Scopus | Cited By in Scopus (8).

[20] K&K Associates. Thermal Network Modeling Handbook. Westminster: K&K Associates; 2000.

[21] Takami KM, Mahmoudi J. Numerical modeling of heat generation and distribution in the core and winding of power transformers. International Journal of Emerging Electric Power Systems 2008;9(2):1–20. article 7, [Full Text via CrossRef].

[22] Popa C, Cojocariu I, Barba N, Pentiuc R. Thermal nodal model for single-phase dry type transformers. In: Graur A, Pentiuc SG, Potorac AD, Filote C, Mahalu G, editors. Development and application systems. DAS 2000: proceedings of the 5th international conference on development and application systems. Suceava, Romania: Suceava: Editura Musatinii; 2000 May 18–20. p. 361–6.

[23] Popescu D, Ungurean F, Guerrero AH. Simulation models for the analysis of space heat consumption of buildings. 11th Conference on process integration, Modelling and Optimization for energy saving and Polution Reduction, Prague. Energy Journal 2009;34(10):1447–53. Article | PDF (323 K) | Wiew Record in Scopus | Cited By in Scopus (4).

[24] Lund H, Möeller B, Mathiesen BU, Dyrelund A. The role of district heating in future renewable energy systems. Energy Journal 2010;35(3):1381–90. Article | PDF (1089 K) | Wiew Record in Scopus | Cited By in Scopus (6).

[25] Nitu C, Dobrescu AS. The role of Weather Indicators in energy consumption. Advances in Electrical and Computer Engineering 2008;8(1):17–20 [Full Text via CrossRef].

[26] Zhu L, Hurt R, Correia D, Boehm R. Detailed energy saving performance analyses on thermal mass walls demonstrated in a zero energy house. Energy and Buildings 2009;41(3):303–10. Article | PDF (1734 K) | Wiew Record in Scopus | Cited By in Scopus (3).

[27] Heiselberg P, Brohus H, Hesselholt A, Rasmussen H, Seinre E, Thomas S. Application of sensitivity analysis in design of sustainable buildings. Renewable Energy 2009;34(9):2030–6. Article | PDF (396 K) | Wiew Record in Scopus | Cited By in Scopus (3).

Glossary

$W_{electric}$: electric energy absorbed by the converter from the supply source (W);
$W_{useful\ electrical}$: useful electric energy transferred to a load (W);
$\Delta W_{thermal\ loss\ c-w}$: energy losses due to windings and magnetic core in the case of static converters (W);
$W_{useful\ mechanical}$: useful mechanical energy in the leading axle (W);
$\Delta W_{thermal\ loss\ r-s}$: energy losses in rotor and stator windings of dynamic converters (W);
$\Delta W_{mechanical\ loss}$: energy losses due to friction of mechanical subparts (W);
$W_{useful\ thermal\ sec}$: useful thermal energy generated in the massive secondary circuit of the static converter (W);

$W_{useful\ thermal\ c-w}$: useful thermal energy generated in the magnetic circuit and in the primary winding, in the case of static converters (W);
$W_{useful\ thermal\ r-s}$: useful thermal energy generated in the rotor and stator winding of the dynamic converter (*W*);
$u_1 = \sqrt{2}U_1 \sin\omega t$: instantaneous primary voltage (V);
u_2: secondary voltage (V);
N_1, N_2: primary and secondary windings turns;
i_1, i_2: windings primary and secondary currents (A);
R_1, R_2: windings electrical resistance (Ω);
L_{1s}, L_{2s}: windings leakage inductances (H);
i_m: magnetization current (A);
$\Re_{1in}$, $\Re_{2in}$: magnetic reluctances that correspond to windings magnetic flux leakage, inside window core (H^{-1});
$\Re_{1out}$, $\Re_{2out}$: magnetic reluctances that correspond to windings magnetic flux leakage, outside window core (H^{-1});
k_{f1}, k_{f2}: form factor that corrects the leakage windings inductances;
h: height of primary winding (m);
g_1: primary winding thickness (m);
g_2: secondary winding thickness (m);
g_m: magnetic core width (m);
g_a: distance between exterior surface of primary winding (inductor) and interior surface of secondary (m);
g_{a1}: distance between central column of magnetic core and interior surface of primary winding (m);
D_1: primary winding inner diameter (m);
D_2: secondary winding inner diameter (m);
$J = \frac{N \cdot i}{h}$: linear current density in winding (Am^{-1});
$dI = J \cdot dz$: current into elementary element dz (A);
$\underline{r}$: distance between element dz to point P(Y, jZ) (m);
$\underline{H_{0y}}$, $\underline{H_{0z}}$: maximum magnetic field intensity components at secondary winding surface (A/m);
r_i: inner radius of secondary winding (m);
r_e: exterior radius of secondary winding (m);
P_{axis}: local active power induced in secondary winding about the considered axis (W);
C: heat capacity, assigned to a thermal node (J/K);
T: temperature assigned to a node in thermal network model (K);
C: matrix of heat capacities derived from thermal network model (J/K);
G: matrix of thermals conductances derived from thermal network model (W/K);
P: the vector of heat input derived from power sources model (W);
P_1: total active power absorbed by converter (W);
P_2: active power developed in the secondary winding of electro-thermal converter (W);
P_{1Cu}: Joule-Lenz loss in inductor, primary winding (W);
P_{1Fe}: iron core loss (W);
P_{2Fe}: secondary winding ferromagnetic material loss (only when this is made of iron) (*W*).

Greek symbols
ϕ: magnetic flux (Wb);
ω: angular frequency ($rads^{-1}$);
α_1: angle corresponds to a half of the primary windings area found in the inner area of the window core (°);
α_2: angle corresponds to a half of the secondary windings area found in the inner area of the window core (°);
α_R: resistivity temperature coefficient ($°C^{-1}$)
μ_0: magnetic permeability of vacuum (Hm^{-1});
μ_{r1}: magnetic core relative permeability;
μ_2: secondary winding magnetic permeability (Hm^{-1});
δ: penetration depth (m);
σ: material electrical conductivity (S/m);
ρ_0: resistivity coefficient at 0 °C (Ωm);
θ_{sec}: secondary temperature (°C);
Δu: infinitesimally length considered in the massive wall of secondary winding (along *Oy* axis) (m);
Θ_1: vector of temperatures, main variables (° C);
Θ_2: vector of temperatures, secondary variables (° C);
η_e: efficiency for electro-thermal converter.